

First-Principles investigations of the thermoelectric properties of CoHfSi *half*-Heusler alloy

Sadhana Matth, S. Pandey, Himanshu Pandey*

*Condensed Matter Low-Dimensional Systems Laboratory, Department of Physics,
Sardar Vallabhbhai National Institute of Technology, Surat-395007, Gujarat, India*

*hp@phy.svnit.ac.in

Abstract

In this paper, density functional theory is performed to investigate the phonon dispersion, elastic, thermodynamic, and thermoelectric properties of half-Heusler alloy CoHfSi in Quantum espresso software using First-principles calculations. The alloy is found to be semiconducting with a band gap of 1.13 eV. The material is mechanically stable, as satisfied by the elastic properties in the thermo_pw package using Born-Huang stability criteria. Positive phonon frequencies determine that the material is dynamically stable. BoltzTrap code is utilized to determine the thermoelectric properties. The higher value of the Seebeck coefficient (150 μ V/K-250 μ V/K) is required for more conversion efficiency. zT increases with the temperature increase and reaches a maximum value of 3 at 850K.

Introduction

The pressing issues of global warming and energy generation require us to accelerate our pace of energy production while minimizing CO₂ emissions and reducing reliance on finite fossil fuel resources. Developing advanced renewable energy technologies has become a paramount global priority to meet the energy demands of a growing world population. Although renewable sources such as wind, solar, tidal, biomass, and geothermal energy offer promising solutions, their intermittent nature and dispersed availability pose challenges compared to the centralized power plants currently dominating the electrical energy landscape. Therefore, it is crucial to explore strategies that enhance the reliability and accessibility of these renewable energy sources. Nevertheless, a considerable proportion of energy is expended as heat through the combustion of fossil fuels and other traditional and renewable energy sources. If this energy could be used and converted into electricity with optimal effectiveness and efficiency, it would serve as a promising prospective electrical power source. Intensive research into developing and enhancing thermoelectric materials has been motivated by the increasing demand for clean energy solutions and the necessity to enhance the efficiency of current energy systems [1] [2] [3] [4] [5].

Thermoelectric materials have received much attention due to the growing demand for renewable energy resources to convert waste heat from various industrial machines to usable electricity using the Seebeck effect. However, the low conversion efficiency of these materials has been an acritical hindrance to replacing old power generation technologies [6] [7]. The efficiency of thermoelectric materials can be calculated using a dimensionless quantity known as a figure of merit (zT), which takes into account the Seebeck coefficient (S), electrical

conductivity (σ), and thermal conductivity (κ) consisting of electronic (κ_e) as well as phonon (κ_{ph}) parts.

$$zT = \frac{\sigma S^2}{(\kappa_e + \kappa_{ph})} T$$

Here, T stands for temperature. Inherent trade-offs between these factors provide the challenge in designing high-performance thermoelectric materials. Materials with a higher value of zT provide more conversion efficiency. To maximize zT , a balance between the numerator σS^2 , also known as the power factor, and the denominator κ is needed to maintain. Due to their ability to produce significant thermopower at high temperatures, non-toxic elements, ternary half-Heusler alloys have thus become more and more well-liked among TE materials.

Heusler alloys are a class of thermoelectric (TE) materials, and they have gained significant attention because of their fascinating electrical transport properties and rich elemental combinations. An inherent benefit of Heusler alloys in thermoelectric applications is their capacity to attain high power factors while preserving comparatively low heat conductivity. This is mainly attributed to the unique crystal structures of these materials, which may be precisely controlled to increase phonon scattering and decrease lattice thermal conductivity without causing a substantial decrease in electrical conductivity. *Half-Heusler* (HH) alloys typically comprise transition metals (X and Y) and main group elements (Z). The crystal structure of these alloys is non-centro symmetric, with X and Z atoms forming a zinc-blende structure and Y atoms filling the voids. The bonding between X and Z atoms mainly creates a semiconducting band gap [8]. Heusler alloys are being investigated to tailor band gap and the Fermi level (E_F), which helps design *p-type* and *n-type* semiconducting materials from the same alloy with comparable physical properties. This minimizes the lattice mismatch where different *p-type* and *n-type* materials and respective devices can be fabricated using the same parent alloy, offering a higher energy conversion efficiency than a TE device. So far, most of the efforts have been concentrated on intensifying the TE performance of *n-type* HH alloys. However, there are few studies on *p-type* HH alloys, and zT values are still relatively low. Therefore, it is essential and necessary to explore potential *p-type* HH alloys or enhance the performance of existing *p-type* HH alloys [9] [10] [11] [12]. The zT of *p-type* FeNbSb-based alloys recently reached a high value of 1.5 at 1200K [13] [14], whereas the zT of *n-type* XNiSn ($X = \text{Ti, Zr, and Hf}$) alloys reached its maximum value of 1.0 at 820K, and that of *p-type* XCoSb ($X = \text{Ti, Zr, and Hf}$) alloys hits 1 at 1073K [15] [16].

Researchers have been searching for newer and newer materials to address these issues. Various families of materials, such as Clathrates[17], Chalcogenides[18], Skutterudites[19], Heusler alloys [20] [21] [22] [23] [24], especially cobalt-based Heusler alloys and many others, are being investigated theoretically as well as experimentally. Due to robustness, low cost, thermodynamic stability, non-toxic [25], and a multi-functional class of materials, Heusler alloys have been extensively investigated and synthesized for various energy-based applications such as spintronics [26] [27] [28] lithium-ion batteries [29] [30] catalyst [31]

sensor [32] [33] shape memory [34] [35] energy harvesting [36] [37] and magnetic cooling [38] etc.

Cobalt, hafnium, and silicon-based alloys have significantly progressed in thermoelectric energy conversion applications. To enhance the zT value for thermoelectric applications, we have incorporated Co, Hf, and Si into the CoHfSi HH alloy. So far, theoretical or experimental data regarding this material have been absent in the literature. The main objective of this work is to examine the electrical configuration and the elastic, phonon, and thermoelectric properties of Co-based intermetallic HH alloy. Before achieving any practical device thermoelectric applications and enhancements in figure-of-merit, it is essential to comprehend the material, its characteristics, correlation, and performance through first-principles calculations that can offer valuable and early suggestions. The present study investigates the electronic structure and thermoelectric properties of CoHfSi HH alloys. The results derived from this material indicate that it has the potential to be a suitable material for thermoelectric applications.

Computational Details

We have optimized the crystal structure of CoHfSi in the cubic phase (space group $F\bar{4}3m$, 216) within generalized gradient approximation [39] to estimate the ground state energy, electronic, and thermoelectric properties using first-principle calculation as implemented in the Quantum Espresso package [40]. Ultrasoft pseudo-potentials are used to study the interaction between core and valence electrons. The *cut-off* corresponding to kinetic energy for wave functions and charge densities are set to be 100 and 900Ry, respectively. In the Brillouin zone, a k -point mesh of $12 \times 12 \times 12$ and a much denser mesh of $40 \times 40 \times 40$ are considered with a convergence threshold criterion of 10^{-6} for self-consistent and non-self-consistent calculations. A semi-classical code based on Boltzmann transport formalism, BoltzTrap [41], is used to calculate the thermoelectric properties for CoHfSi *half*-Heusler alloy. Three primary factors are considered for determining zT : electrical conductivity, thermal conductivity, and the Seebeck coefficient. The Seebeck coefficient, electrical conductivity, and lattice part of thermal conductivity using Slack's [42] formula can be determined by using mathematical equations (1) - (3) [43].

$$S_{\alpha\beta}(T, \mu) = \frac{1}{eT\Omega\sigma_{\alpha\beta}} \int \sigma_{\alpha\beta}(\epsilon)(\epsilon - \mu) \left[-\frac{\partial f_0(T, \epsilon, \mu)}{\partial \epsilon} \right] d\epsilon \quad (1)$$

$$\sigma_{\alpha\beta}(T, \mu) = \frac{1}{\Omega} \int \sigma_{\alpha\beta}(\epsilon) \left[-\frac{\partial f_0(T, \epsilon, \mu)}{\partial \epsilon} \right] d\epsilon \quad (2)$$

$$k_L = \frac{A_L}{T}, \quad A_L = A \frac{\bar{M}_{CoHfSi} n^{1/3} \delta \Theta^3}{\gamma^2} \quad (3)$$

The primitive cell's volume is denoted by Ω , the charge by e , and the Fermi-Dirac distribution function by f_0 . \bar{M}_{CoHfSi} , $n^{1/3}$, Θ^3 , γ^2 , δ represents the average atomic mass of the material, the total number of atoms in the unit cell, Debye temperature for acoustic phonon frequencies, Gruneisen parameter, volume of unit cell per atom, and further A is a constant quantity can be

calculated using the formula $A = \frac{2.43 \times 10^{-8}}{1 - \frac{0.514}{\gamma} + \frac{0.228}{\gamma^2}}$. Gruneisen parameter is a dimensionless quantity, and varies with temperature, and can be calculated using the Poisson ratio(ν), $\gamma = \frac{3}{2} \left[\frac{1+\nu}{2-3\nu} \right]$. To verify the result produced by Slack's equation, we have calculated the lattice thermal conductivity using the Phono3py code [44]. The relaxation time(τ) parameter is required to calculate the electrical conductivity per relaxation time and the electronic part of thermal conductivity per relaxation time, $\tau = \frac{A}{T^{3/2}}$, $A = \frac{2\sqrt{2}\pi C \hbar^4}{3(k_B m_d^*)^{3/2} E^2}$, where C , \hbar , k_B , m_d^* , and E represents elastic constants, reduced Planck constants, Boltzmann constant, effective mass, and deformation potential. The Voigt approximation is used in the thermo_pw program to evaluate thermodynamical characteristics and elastic coefficients (C_{11} , C_{12} , and C_{44}). Determining the Debye temperature (θ_D) requires the calculations of both the average sound velocity (v_m) and the longitudinal (v_l) and transverse (v_t) wave velocity. These parameters can be computed using the following equations [23] [22] [9].

$$\theta_D = \frac{\hbar}{k_B} \left[\frac{3n}{4\pi} \left(\frac{N_A \rho}{M} \right) \right]^{1/3} v_m, \quad v_m = \left[\frac{1}{3} \left(\frac{2}{v_t^3} + \frac{1}{v_l^3} \right) \right]^{-1/3}, \quad v_t = \left(\frac{4G+B}{3\rho} \right)^{1/2}, \quad v_l = \left(\frac{G}{\rho} \right)^{1/2}$$

Result and Discussion

Structural properties

XYZ is the chemical formula of the half-Heusler alloys derived by F. Heusler, having a stoichiometric ratio of 1:1:1. By altering the atomic locations, CoHfSi HH can exhibit three distinct electronic configurations: Phase-1, Phase-2, and Phase-3. Optimized CoHfSi exhibits stability in Phase 1, with atomic locations of Co, Hf, and Si at (0.25, 0.25, 0.25), (0, 0, 0), and (0.5, 0.5, 0.5). An analysis of the relationship between the volume and total energy is presented in our earlier publication [45] and also the crystal structure.

Lattice parameters, formation energy (E_{form}), effective mass, and band gap are presented in Table 1. Formation energy is calculated using the equation:

$$E_{form} = E_{CoHfSi} - (E_{Co} + E_{Hf} + E_{Si}) \quad (4)$$

Here, E_{CoHfSi} represents the total ground state energy of the alloy in its unit cell, and E_{Co} , E_{Hf} , and E_{Si} is the total energy of the individual atom in its ground state for isolated atom. Negative formation energy is observed, and it represents that the material is thermodynamically stable [10].

Table 1: Calculated lattice parameter (a), the effective mass of hole (m_h^*) and electron (m_e^*) computed at VBM and CBM in terms of rest mass (m_e) of free electron, formation energy (E_f), and band gap (E_g) for CoHfSi alloy.

a (Å)	$m_h^*(m_e)$	$m_e^*(m_e)$	E_f (eV)	E_g (eV)
5.77	0.3001	1.208	-21.375	1.132

Phonon properties

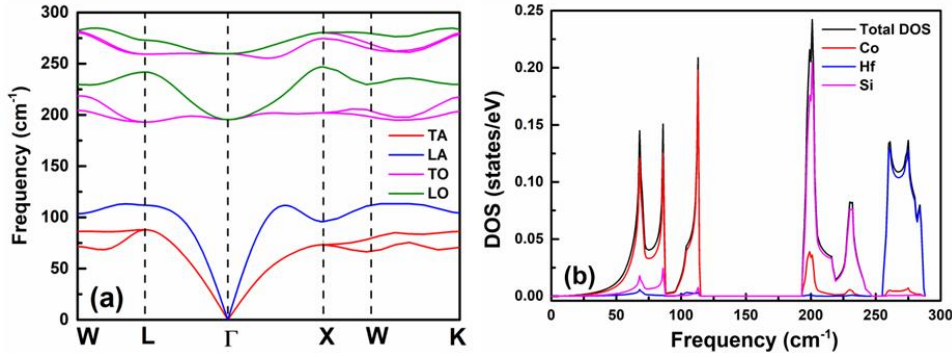


Figure 1: (a, b) Phonon band structure and (c, d) phonon density of states estimated for CoHfSi unit cell

Dynamical stability is another method to determine the stability of the material. The phonon dispersion curve and phonon density of states (PhDOS) are presented in Fig. 1(a, b). The absence of imaginary phonon frequency along the high symmetry k-points ($W \rightarrow L \rightarrow \Gamma \rightarrow X \rightarrow W \rightarrow K$) in the range of $-\pi/2$ to $\pi/2$ determines the stability of the material. The crystal structure of HH alloy contains three atoms in the unit cell, which leads to nine phonon branches, out of which three belong to acoustic branches lie in the low-frequency range, and six belong to optical phonon branches lie in the high-frequency range. The three acoustic branches comprise one longitudinal acoustic (LA) and two transverse acoustic (TA) modes. In contrast, optical branches comprise 2 LO and 4 TO. Separation between the optical and acoustic branches plays a vital role in lattice thermal conductivity. The smaller the band gap between these branches, the lower the lattice thermal conductivity, which helps attain a high zT value [46] [20]. From the phonon density of states, the Co atom dominates at a lower frequency range, whereas silicon and hafnium dominate in the high-frequency range.

Elastic properties

Table 2: Calculated elastic constants C_{11} , C_{12} , C_{44} in the units of GPa, bulk modulus (B), Young's modulus (Y), shear modulus (G), Poisson ratio (P), debye temperature (θ_D), pugh ratio (B/G), Cauchy pressure, and Anisotropy constant (A).

C_{11} (GPa)	C_{12} (GPa)	C_{44} (GPa)	B (GPa)	Y (GPa)	G (GPa)	P	θ_D (K)	B/G	Cauchy pressure	A
242.23	98.01	45.19	146.08	148.87	55.96	0.33	52.82	2.61	242.23	0.63

Before utilizing any material in any application, it is imperative to verify its stability. Several parameters, including the interatomic distance between the atoms, bond length, and arrangement of atoms in the crystal arrangement, influence the stability of a material. The mathematical calculation of elastic properties is the most fundamental method to ascertain the stability of a material. Elastic characteristics provide information on the stability of a material and its mechanical response to an external force. We computed the elastic properties of this face-centered cubic (*fcc*) CoHfSi material using the thermo_pw software. C_{11} , C_{12} , and C_{44} are three independent elastic constants for a cubic system, which indicates resistance under linear compression and transverse expansion under the application of stress and hardness of the material and are presented in Table 2. If these three elastic constants adhere to the stability

criterion by Born Huang [47], then this material is considered stable. Born Huang's stability criteria are:

$$C_{11} > 0$$

$$C_{44} > 0$$

$$C_{11} - C_{12} > 0$$

$$C_{11} + 2C_{12} > 0$$

The elasticity criterion indicates that the material maintains mechanical stability. Elastic constants indicate that C_{11} is higher than C_{12} and C_{44} , suggesting that a more robust external force is necessary to compress the compound along the x -axis compared to the y - and z -axes. Additional elastic properties of the material, such as the shear modulus (G), bulk modulus (B), Young's modulus (Y), Poisson's ratio (ν), Debye temperature, Cauchy pressure (CP), and Anisotropy ratio can be determined using these three independent elastic constants. Bulk modulus (B) determines how much a material resists its volume change. Young's modulus (Y) and shear modulus (G) determine the material's capacity to resist change in length when the material is stretched or compressed in one direction and plastic deformation. Poisson ratio, Pugh ratio, and Cauchy pressure determine whether the material is ductile or brittle. The Poisson ratio is 0.33, representing the ductile material under investigation. If the ratio is less than 0.28, the material is brittle. Cauchy pressure (CP) is another critical parameter that determines the brittleness and ductile nature of the material. The difference between the C_{12} and C_{44} estimates CP. If C_{12} is greater than C_{44} , the material is ductile; vice-versa, the material is brittle. A positive value of Cauchy pressure determines that bonding between the atoms is ionic. Otherwise, it is covalent bonding. Pugh ratio (B/G) is calculated by the ratio of bulk modulus and shear modulus; if the B/G ratio is greater than 1.75, then the material is ductile in nature; otherwise, it is brittle. Our calculated results represent that the Pugh ratio is 2.61, which confirms that the investigated alloy is ductile [46]. The Debye temperature (θ_D) represents the temperature associated with the highest normal mode of vibration in a crystal and provides valuable information about the lattice vibrations. Moreover, it also offers insight into the thermodynamics of the material based on its elastic properties, as it is an indicator of the covalent bond's strength within the crystal structure. The estimated values of θ_D are well above 300 K, suggesting a strong covalent bonding between atoms. The anisotropy factor is another vital parameter that determines whether a material under strain has the same physical properties in every direction or not. If a material's anisotropy value is precisely 1, then the material is isotropic in nature, otherwise it is anisotropic. For our calculated results, A is less than 1, which means the alloy is anisotropic [22] [47].

Thermoelectric properties

The thermoelectric characteristics of the half-Heusler alloy CoHfSi for the spin-up channel is covered in this section. Equations (1)-(3) are used in the BoltzTrap code to compute transport parameters, including electrical conductivity (σ), thermal conductivity ($\kappa_e + \kappa_L$), and Seebeck coefficient (S). The capability of CoHfSi alloy for thermoelectric applications is assessed by calculating these properties as a function of temperature, and chemical potential.

The Seebeck effect expresses the ratio of voltage created between a material's ends when it is exposed to a temperature difference. Because of the temperature difference, moving charge carriers like electrons or holes create an electrical current. Figure 4(a) demonstrates the relationship between S and temperature. The Seebeck coefficient exhibits a linear increase with temperature, reaching a maximum limit and gradually decreasing up to 700K. A reduction in the Seebeck coefficient occurs due to an increase in thermally excited charge carriers and bipolar transport, and beyond 700K, the Seebeck coefficient approaches a constant value. At high temperatures, bipolar transport was significantly increased because thermal agitation led to the production of minority carriers. Conversely, at high temperatures, there are fewer unoccupied states above the Fermi level than at low temperatures. The combined effect of these processes led to a lower Seebeck coefficient [48]. The variation in the Seebeck coefficient with temperature is contingent upon the effective mass of holes and electrons (m^*) near the Fermi level, which can be determined using the following formula.

$$S = \frac{8\pi^2 k_B^2}{3eh^2} m^* T \left(\frac{\pi}{3n} \right)^{2/3} \quad (5)$$

Here, the physical meaning of these quantities are as follows: Boltzmann constant (k_B), temperature (T), electronic charge of hole and electrons (e), Planck constant (h), and carrier concentration (n). Nevertheless, the effective mass (m^*) of free charge carriers (electrons and holes) can be estimated from the curvature of CBM and VBM using wave vector (k) and reduced Planck constant (\hbar), and Kohn–Sham energy eigenvalue (E) as $m^* = \hbar^2 / (\partial^2 E / \partial k^2)$. It should be noted that the positive value of Seebeck across the entire range of temperature for spin-up states indicates that holes are responsible for conduction in this material because charges carried by thermally excited holes begin to dominate. For a good thermoelectric material, the value of the Seebeck coefficient lies in the range of 150-200 $\mu\text{V/K}$. The substantially higher number of states in the valence band (near the Fermi level) than in the conduction band may be one of the reasons for this higher Seebeck voltage [49] [50].

S in the BoltzTrap code is not affected by relaxation time, but the electronic components of thermal conductivity and electrical conductivity are. Thermoelectric materials with optimal characteristics should have high electrical conductivity, and low thermal conductivity is required. The electrical conductivity is significantly influenced by temperature. The variation in electrical conductivity per relaxation time over different temperature ranges is illustrated in Fig. 4(b). The electrical conductivity confirms the CoHfSi alloy's semiconducting nature, which gradually increases with temperature. The increased electrical conductivity results from diminished scattering at elevated temperatures, illustrating the material's degenerate semiconductor characteristics [51] [52].

Total thermal conductivity is the sum of two components, electronic and lattice thermal conductivity, for every material. Fig. 4(c) shows the variation of electronic thermal conductivity as a function of increasing temperature range. Electronic thermal conductivity progressively increases with an increase in temperature. This is due to the increased charge carriers at elevated temperatures, which improves electronic thermal conductivity. One of the causes of the temperature-dependent increase in lattice thermal conductivity is an increase in phonon diffusion [50]. According to Wiedemann Franz's law ($K = \sigma LT$), the identical behavior

seen for both quantities (electronic thermal conductivity and electrical conductivity) indicates that they are directly proportional to one another.

Figure 4(d) illustrates the variation of lattice thermal conductivity with temperature. We also calculated the lattice thermal conductivity with the PHONO3PY algorithm for the CoHfSi alloy to validate the result's precision derived from Slack's equations. Figure 4(d) illustrates a disparity in lattice thermal conductivity at low temperatures; however, at elevated temperatures, the lattice thermal conductivity values agree with each other. Lattice thermal conductivity is higher at lower temperatures due to the increased mean free path at lower temperatures, which allows greater heat transfer by phonons, resulting in higher lattice thermal conductivity. At elevated temperatures, phonon-phonon scattering prevails, resulting in diminished mean free path, hence reducing the thermal conductivity of phonons. Minimal thermal conductivity is necessary to attain a superior figure of merit [53].

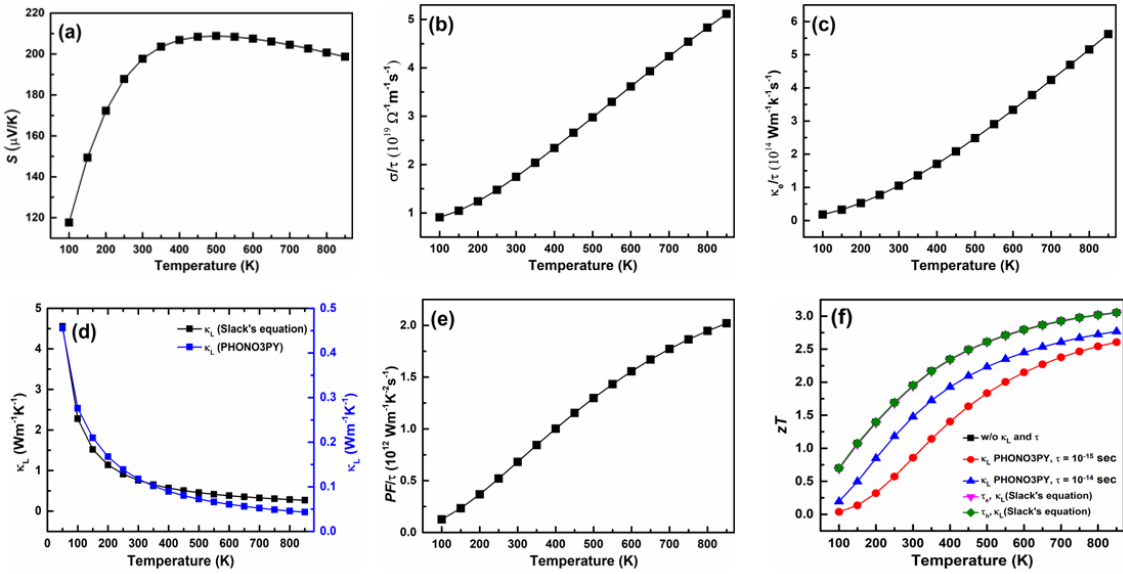


Figure 2: Variation of a) Seebeck coefficient, b) electrical conductivity per relaxation time, c) electronic thermal conductivity per relaxation time, d) lattice thermal conductivity, e) power factor per relaxation time, f) zT with temperature for the CoHfSi unit cell.

The thermoelectric power factor denotes the combined influence of the Seebeck coefficient and electrical conductivity, as seen in Fig 4 (e). PF exhibits a correlation with the Seebeck trend. PF increases with increasing temperatures. A higher power factor indicates that a greater amount of current and voltage is generated. A higher power factor is required to convert waste heat into useful work. In Figure. 4 (f), we plotted the zT variation with temperatures ranging from 100K to 850K. Here, the lattice part of thermal conductivity and relaxation time are included to determine the zT . zT shows a similar kind of behavior as Seebeck. Here, the lattice part of thermal conductivity is calculated using Slack's equation and phono3py code. Relaxation time is calculated using the equation presented in the computational details section, and a fixed relaxation time of 10^{-15} sec and 10^{-14} sec is considered to estimate the zT . zT increases with the temperature increase, which is highly required to achieve a high figure of merit.

The relaxation time refers to the time required for a system to return to equilibrium after being disturbed. Variation of relaxation time (τ) for hole and electron with respect to temperature is presented in Fig. 3. As temperature increases, relaxation time decreases due to increased collision between the electrons and holes and enhanced molecular motion and kinetic energy [54].

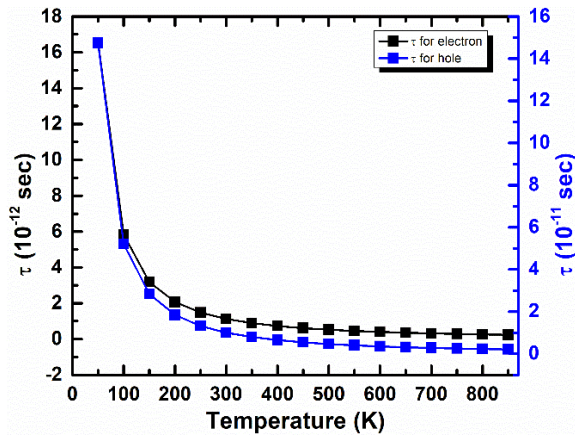


Figure 3: variation of relaxation time with temperature

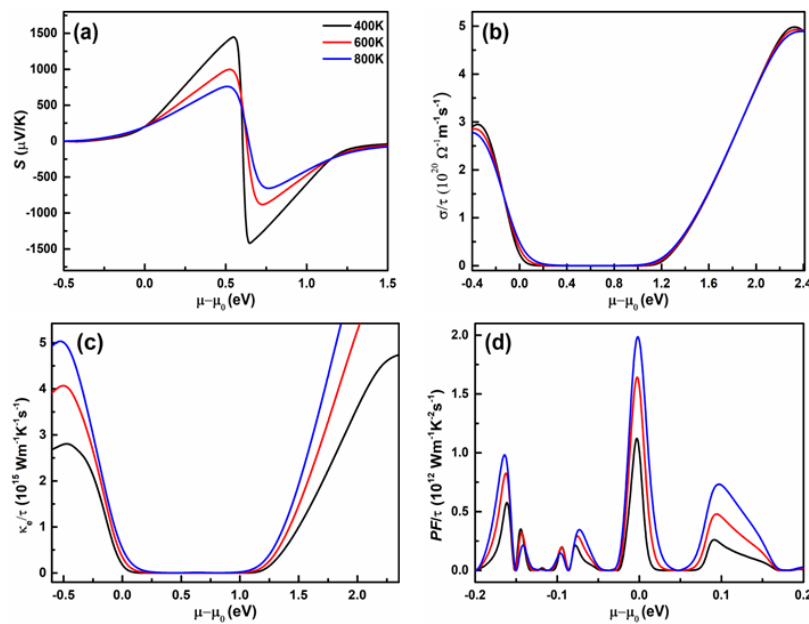


Figure 4: Variation of a) Seebeck coefficient, b) electrical conductivity per relaxation time, c) electronic thermal conductivity per relaxation time, d) power factor per relaxation time with fermi level at 400K, 600K, and 800K for the CoHfSi unit cell.

The Seebeck coefficient is plotted as a function of the chemical potential at 400 K, 600K, and 800 K, as presented in Fig. 4 (a). The peak value of S at 400K for n -type is $1458.20\mu\text{V}/\text{K}$; however, with the increase in temperature, the peak value decreases and reaches $712.58\mu\text{V}/\text{K}$ at 800K. This is due to an increase in thermal energy. There are two peaks at $\mu = 0.55$ eV and 0.64 eV, and when one moves outside of this range, the S rapidly approaches zero. For all ranges of the temperatures, peaks lie in the n -type region ($\mu - \mu_0 > 0$).

Electrical conductivity per relaxation time is plotted in Fig. 4(b) at different temperatures (400K, 600K, and 800K) as a function of chemical potential. Electrical conductivity is observed as zero in the 0.32 to 1 eV range. However, it is observed that where the Seebeck coefficient value has its maximum value, the electrical conductivity is virtually approaching zero at that point. This represents that the behavior of σ and S are completely opposite to each other. As we go away from this range, electrical conductivity increases. This is caused by a low density of charge carriers ($j = \sigma E$), which lowers conductivity and enhances potential difference. Beyond the Fermi level, two peaks exist, one in the *p-type* region and the second in the *n-type* region, respectively, in the *n-type* region, maximum peaks of electrical conductivity are $4.98 \times 10^{20} \Omega^{-1} \text{m}^{-1} \text{s}^{-1}$, $4.92 \times 10^{20} \Omega^{-1} \text{m}^{-1} \text{s}^{-1}$, and $4.89 \times 10^{20} \Omega^{-1} \text{m}^{-1} \text{s}^{-1}$ at 400K, 600K, and 800K, whereas in *p-type* region highest values are $2.94 \times 10^{20} \Omega^{-1} \text{m}^{-1} \text{s}^{-1}$, $2.87 \times 10^{20} \Omega^{-1} \text{m}^{-1} \text{s}^{-1}$, and $2.77 \times 10^{20} \Omega^{-1} \text{m}^{-1} \text{s}^{-1}$. It clearly represents that *n-type* doping dominates over *p-type* doping for the CoHfSi compound due to the lighter effective mass of electrons in the conduction band.

The electronic thermal conductivity κ_e is plotted as a function of the chemical potential at 400 K, 600K, and 800 K, as presented in Fig. 4(c). For *n-type*, CoHfSi has the highest value compared to *p-type* for all temperature ranges. Thermal conductivity decreases with a temperature decrease for both *p-type* and *n-type*, reaching $4.75 \times 10^{15} \text{ Wm}^{-1} \text{K}^{-1} \text{s}^{-1}$ and $2.80 \times 10^{15} \text{ Wm}^{-1} \text{K}^{-1} \text{s}^{-1}$ at 400K. Electronic thermal conductivity is observed as zero in the 0.25 to 1 eV range; approximately σ is zero in the same range. If thermal conductivity and electrical conductivity graphs are compared, then the result shows that both graphs are identical to each other because both quantities are interconnected through the Wiedemann-Franz law.

The variation of the power factor as a function of the chemical potential at different temperature ranges (400 K, 600K, and 800 K) is presented in Fig. 4 (d). The results represent that *p-type* doping dominates over *n-type* doping. Meanwhile, for both *p-type* and *n-type*, its value decreases with a decrease in temperature [55].

Thermodynamic Properties

To determine the thermodynamic or thermal characteristics of CoHfSi, we used the `thermos_pw` software. Calculating thermodynamic properties such as debye heat capacity, debye entropy, debye vibrational energy, and debye vibrational free energy under a temperature range of 100-800K, as given in Fig. 5, provides information about the chemical stability, which further enables the use of those materials in the industry based on their stability [48,49].

Variation of vibrational energy with temperature is presented in Fig 5(a). Vibrational energy comprises many kinds of motion, such as translational, rotational, and vibrational motions. As the temperature increases, these particles move more rapidly, resulting in greater translational, rotational, and vibrational motions. This increase in particle motion contributes to a higher kinetic energy.

Variation of entropy as a function of temperature is represented in the Fig. 5(b). With the increase in temperature, entropy increases, starting with zero. With the increase in temperature, vibration between the atoms increases, increasing the system's internal energy [56].

Figure 5(c) depicts the variation of debye heat capacity and demonstrates how it increases linearly with temperature above 100K. Above 500K, debye heat capacity does not change with temperature, indicating that an anharmonic influence on debye heat capacity is ignored. This represents that the theory of specific heat at low temperatures ($C \propto T^3$) is followed due to an anharmonic effect. The solid elements' molar heat capacity (C_p) is near $3R$, or $25 \text{ J.K}^{-1} \text{ mol}^{-1}$ for monoatomic solids, according to the constant limit displayed in 1819 by Dulong–Petit [29]. Three-atom compounds should have three times the observed molecular weight of monoatomic solids, or $75 \text{ J.K}^{-1} \text{ mol}^{-1}$. The findings are completely consistent with the law proposed by Dulong and Petit. It is reasonable to suppose that the heat capacity stays constant at high temperatures [57] [58].

Figure 5(d) shows that Debye vibrational free energy changes with temperature. Debye vibrational free energy decreases with the increase in temperature. Material with higher negative vibrational energy becomes more thermodynamically stable and has a better thermal response [59].

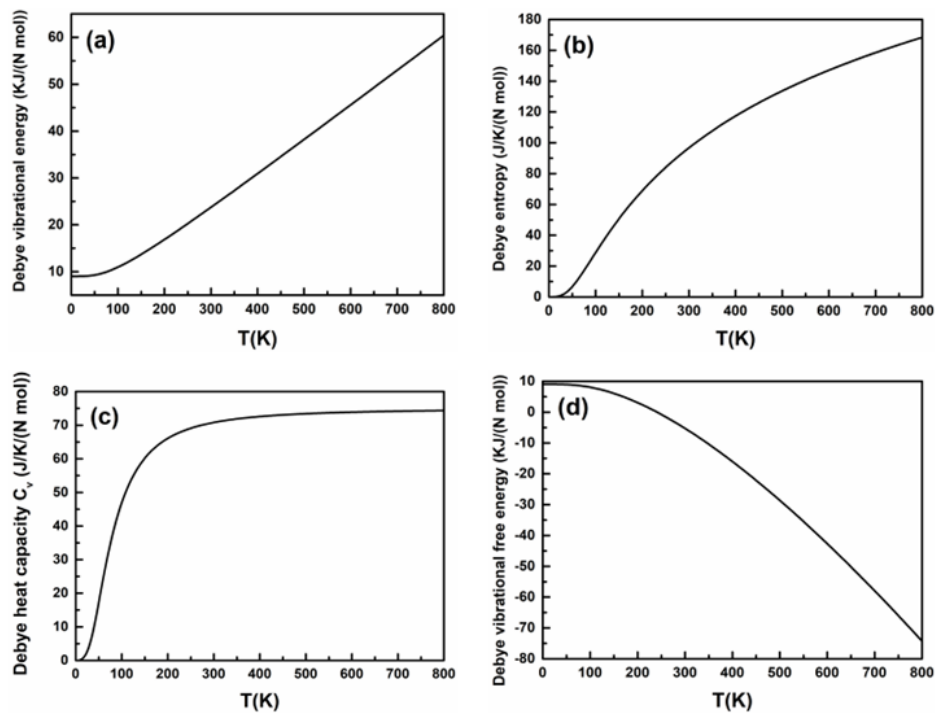


Figure 5: Variation of thermodynamic properties with temperature a) Debye vibrational energy, b) Debye entropy, c) Debye heat capacity, d) Debye vibrational free energy

Electronic fitness function

A general complex band structure's ability to decouple σ and S is gauged by the electrical fitness function (EFF). Using the identity $EFF(t) = (\sigma/\tau)S^2/N^{2/3}$ it is determined. In this case, the inverse scattering rate is given by τ , and N gives the volumetric density of states. Based on first-principles electronic structure calculations and Boltzmann transport theory, this EFF can be computed directly using the constant relaxation time approach [60]. To ascertain the decoupling between the conductivity and the Seebeck coefficient, the electrons and

hole concentrations dependent EFF has been computed in Fig. 6. At various temperatures, the EFF was calculated (400, 600, 800 K). CoHfSi exhibits a considerable decoupling of electrical conductivity and Seebeck coefficient at concentrations closer to 0 cm^{-3} , which suggests that doping is a method of boosting this material's thermoelectric performance [61] [62].

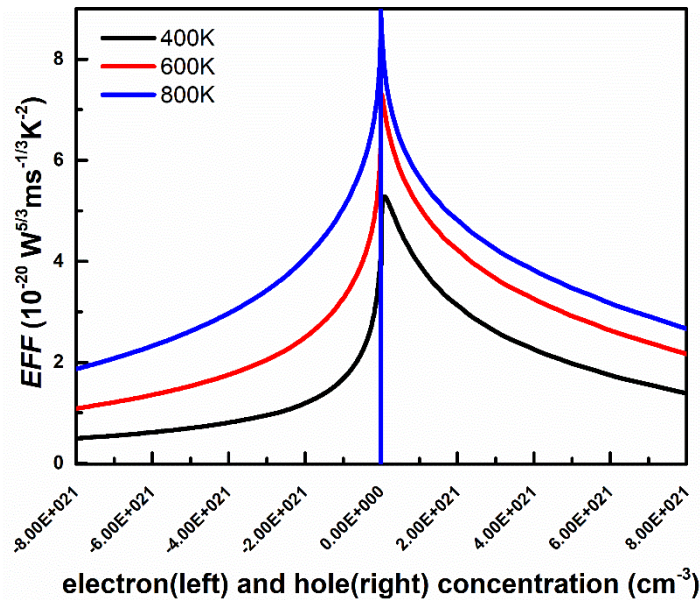


Figure 6: Variation of electronic fitness function as a function of temperature

Conclusion

Based on the Kohan-Sham density functional theory, we have investigated the phonon dispersion, elastic, thermoelectric, and thermodynamic properties of half-Heusler alloy CoHfSi using GGA, PBE functional. Electronic properties determine that the material is semiconducting in nature with an indirect band gap of 1.132 eV between Γ -X. Formation energy, phonon dispersion, and elastic properties determine that the alloy is showing its stability. Seebeck coefficient, which lies in the range of $150 \mu\text{V}/\text{K}$ to $200 \mu\text{V}/\text{K}$, determines this alloy could be a potential candidate for thermoelectric application. The power factor increases with the increase in temperature, which is good for achieving a high figure of merit. zT increases with temperature and reaches a maximum of 3 at 850K.

References

- [1] H. Kim, E. Park, S. J. Kwon, J. Y. Ohm, and H. J. Chang, "An integrated adoption model of solar energy technologies in South Korea," *Renew. Energy*, vol. 66, pp. 523–531, Jun. 2014, doi: 10.1016/j.renene.2013.12.022.
- [2] V. V. Tyagi, N. A. A. Rahim, N. A. Rahim, and J. A. /L. Selvaraj, "Progress in solar PV technology: Research and achievement," *Renew. Sustain. Energy Rev.*, vol. 20, pp. 443–461, Apr. 2013, doi: 10.1016/j.rser.2012.09.028.

- [3] J. Peng, L. Lu, and H. Yang, "Review on life cycle assessment of energy payback and greenhouse gas emission of solar photovoltaic systems," *Renew. Sustain. Energy Rev.*, vol. 19, pp. 255–274, Mar. 2013, doi: 10.1016/j.rser.2012.11.035.
- [4] A. B. Stambouli and E. Traversa, "Solid oxide fuel cells (SOFCs): a review of an environmentally clean and efficient source of energy," *Renew. Sustain. Energy Rev.*, vol. 6, no. 5, pp. 433–455, Oct. 2002, doi: 10.1016/S1364-0321(02)00014-X.
- [5] D. Larcher and J.-M. Tarascon, "Towards greener and more sustainable batteries for electrical energy storage," *Nat. Chem.*, vol. 7, no. 1, pp. 19–29, Jan. 2015, doi: 10.1038/nchem.2085.
- [6] T. Fang, S. Zheng, T. Zhou, L. Yan, and P. Zhang, "Computational prediction of high thermoelectric performance in p-type half-Heusler compounds with low band effective mass," *Phys. Chem. Chem. Phys.*, vol. 19, no. 6, pp. 4411–4417, 2017, doi: 10.1039/C6CP07897D.
- [7] S. V. Faleev, Y. Ferrante, J. Jeong, M. G. Samant, B. Jones, and S. S. P. Parkin, "Heusler compounds with perpendicular magnetic anisotropy and large tunneling magnetoresistance," *Phys. Rev. Mater.*, vol. 1, no. 2, p. 024402, Jul. 2017, doi: 10.1103/PhysRevMaterials.1.024402.
- [8] P. J. Brown, K. U. Neumann, P. J. Webster, and K. R. A. Ziebeck, "The magnetization distributions in some Heusler alloys proposed as half-metallic ferromagnets," *J. Phys. Condens. Matter*, vol. 12, no. 8, pp. 1827–1835, Feb. 2000, doi: 10.1088/0953-8984/12/8/325.
- [9] S. Ahmad Khandy, K. Kaur, S. Dhiman, J. Singh, and V. Kumar, "Exploring thermoelectric properties and stability of half-Heusler PtXSn (X = Zr, Hf) semiconductors: A first principle investigation," *Comput. Mater. Sci.*, vol. 188, p. 110232, Feb. 2021, doi: 10.1016/j.commatsci.2020.110232.
- [10] G. Forozani, A. A. Mohammad Abadi, S. M. Baizae, and A. Gharaati, "Structural, electronic and magnetic properties of CoZrIrSi quaternary Heusler alloy: First-principles study," *J. Alloys Compd.*, vol. 815, p. 152449, Jan. 2020, doi: 10.1016/j.jallcom.2019.152449.
- [11] A. Hori, S. Minami, M. Saito, and F. Ishii, "First-principles calculation of lattice thermal conductivity and thermoelectric figure of merit in ferromagnetic half-Heusler alloy CoMnSb," *Appl. Phys. Lett.*, vol. 116, no. 24, p. 242408, Jun. 2020, doi: 10.1063/1.5143038.
- [12] S. A. Khandy and J.-D. Chai, "Strain engineering of electronic structure, phonon, and thermoelectric properties of p-type half-Heusler semiconductor," *J. Alloys Compd.*, vol. 850, p. 156615, Jan. 2021, doi: 10.1016/j.jallcom.2020.156615.
- [13] C. Fu, T. Zhu, Y. Liu, H. Xie, X. Zhao, "Band engineering of high performance p-type FeNbSb based half-Heusler thermoelectric materials for figure of merit $zT > 1$."
- [14] R. He *et al.*, "Achieving high power factor and output power density in p-type half-Heuslers $\text{Nb}_{1-x}\text{Ti}_x\text{FeSb}$," *Proc. Natl. Acad. Sci.*, vol. 113, no. 48, pp. 13576–13581, Nov. 2016, doi: 10.1073/pnas.1617663113.
- [15] S. Chen, K. C. Lukas, W. Liu, C. P. Opeil, G. Chen, and Z. Ren, "Effect of Hf Concentration on Thermoelectric Properties of Nanostructured N-Type Half-Heusler Materials $\text{Hf}_x\text{Zr}_{1-x}\text{NiSn}_{0.99}\text{Sb}_{0.01}$," *Adv. Energy Mater.*, vol. 3, no. 9, pp. 1210–1214, Sep. 2013, doi: 10.1002/aenm.201300336.
- [16] Y. W. Chai, T. Oniki, and Y. Kimura, "Microstructure and thermoelectric properties of a $\text{ZrNi}_{1.1}\text{Sn}$ half-Heusler alloy," *Acta Mater.*, vol. 85, pp. 290–300, Feb. 2015, doi: 10.1016/j.actamat.2014.11.042.
- [17] J. L. Cohn, G. S. Nolas, V. Fessatidis, T. H. Metcalf, and G. A. Slack, "Glasslike Heat Conduction in High-Mobility Crystalline Semiconductors," *Phys. Rev. Lett.*, vol. 82, no. 4, pp. 779–782, Jan. 1999, doi: 10.1103/PhysRevLett.82.779.
- [18] W. M. Yim and F. D. Rosi, "Compound tellurides and their alloys for peltier cooling—A review," *Solid-State Electron.*, vol. 15, no. 10, pp. 1121–1140, Oct. 1972, doi: 10.1016/0038-1101(72)90172-4.
- [19] G. S. Nolas, J. L. Cohn, and G. A. Slack, "Effect of partial void filling on the lattice thermal conductivity of skutterudites," *Phys. Rev. B*, vol. 58, no. 1, pp. 164–170, Jul. 1998, doi: 10.1103/PhysRevB.58.164.

- [20] D. R. Jaishi, N. Sharma, B. Karki, B. P. Belbase, R. P. Adhikari, and M. P. Ghimire, "Electronic structure and thermoelectric properties of half-Heusler alloys NiTZ," *AIP Adv.*, vol. 11, no. 2, p. 025304, Feb. 2021, doi: 10.1063/5.0031512.
- [21] G. Ding, G. Y. Gao, and K. L. Yao, "Examining the thermal conductivity of the half-Heusler alloy TiNiSn by first-principles calculations," *J. Phys. Appl. Phys.*, vol. 48, no. 23, p. 235302, Jun. 2015, doi: 10.1088/0022-3727/48/23/235302.
- [22] J. W. Wafula, J. W. Makokha, and G. S. Manyali, "First-principles calculations to investigate structural, elastic, electronic and thermodynamic properties of NbCoSn and VRhSn Half-Heusler compounds," *Results Phys.*, vol. 43, p. 106132, Dec. 2022, doi: 10.1016/j.rinp.2022.106132.
- [23] K. Kaur and R. Kumar, "Giant thermoelectric performance of novel TaIrSn Half Heusler compound," *Phys. Lett. A*, vol. 381, no. 44, pp. 3760–3765, Nov. 2017, doi: 10.1016/j.physleta.2017.09.043.
- [24] A. Shukla, S. Matth, S. S. A. Warsi, and H. Pandey, "Investigation on Co-based half-Heusler alloy: A DFT approach," *Mater. Today Proc.*, p. S2214785323028225, May 2023, doi: 10.1016/j.matpr.2023.05.196.
- [25] M. Mitra *et al.*, "Conventional Half-Heusler alloys advance state-of-the-art thermoelectric properties," *Mater. Today Phys.*, vol. 28, p. 100900, Nov. 2022, doi: 10.1016/j.mtphys.2022.100900.
- [26] H. Pandey, P. C. Joshi, R. P. Pant, R. Prasad, S. Auluck, and R. C. Budhani, "Evolution of ferromagnetic and spin-wave resonances with crystalline order in thin films of full-Heusler alloy Co₂MnSi," *J. Appl. Phys.*, vol. 111, no. 2, p. 023912, Jan. 2012, doi: 10.1063/1.3677996.
- [27] I. Galanakis, K. Özdoğan, and E. Şaşıoğlu, "Spin-filter and spin-gapless semiconductors: The case of Heusler compounds," *AIP Adv.*, vol. 6, no. 5, p. 055606, May 2016, doi: 10.1063/1.4943761.
- [28] H. Pandey, R. Prasad, and R. C. Budhani, "Correlation between Site Disorder and Magnetic Moment in Full-Heusler Co₂ MnSi," in *Proceedings of the International Conference on Strongly Correlated Electron Systems (SCES2013)*, Tokyo, Japan: Journal of the Physical Society of Japan, Jun. 2014. doi: 10.7566/JPSCP.3.017037.
- [29] J. H. Park, D. H. Jeong, S. M. Cha, Y.-K. Sun, and C. S. Yoon, "Electrochemical behaviour of Heusler alloy Co₂MnSi for secondary lithium batteries," *J. Power Sources*, vol. 188, no. 1, pp. 281–285, Mar. 2009, doi: 10.1016/j.jpowsour.2008.11.094.
- [30] A. Shukla, S. Pandey, and H. Pandey, "First-principle calculations on Li₂ CuSb : A novel material for lithium-ion batteries," *Energy Storage*, vol. 5, no. 2, p. e357, Mar. 2023, doi: 10.1002/est2.357.
- [31] T. Kojima, S. Kameoka, and A.-P. Tsai, "The emergence of Heusler alloy catalysts," *Sci. Technol. Adv. Mater.*, vol. 20, no. 1, pp. 445–455, Dec. 2019, doi: 10.1080/14686996.2019.1598238.
- [32] M. V. Lopes *et al.*, "Modulating the Spin Seebeck Effect in Co₂FeAl Heusler Alloy for Sensor Applications," *Sensors*, vol. 20, no. 5, p. 1387, Mar. 2020, doi: 10.3390/s20051387.
- [33] A. Mahendra *et al.*, "Shaping Perpendicular Magnetic Anisotropy of Co₂MnGa Heusler Alloy Using Ion Irradiation for Magnetic Sensor Applications," *Sensors*, vol. 23, no. 9, p. 4564, May 2023, doi: 10.3390/s23094564.
- [34] P. Entel *et al.*, "Modelling the phase diagram of magnetic shape memory Heusler alloys," *J. Phys. Appl. Phys.*, vol. 39, no. 5, pp. 865–889, Mar. 2006, doi: 10.1088/0022-3727/39/5/S13.
- [35] M. Siewert *et al.*, "Designing shape-memory Heusler alloys from first-principles," *Appl. Phys. Lett.*, vol. 99, no. 19, p. 191904, Nov. 2011, doi: 10.1063/1.3655905.
- [36] M. Lallart *et al.*, "Heusler alloy-based heat engine using pyroelectric conversion for small-scale thermal energy harvesting," *Appl. Energy*, vol. 288, p. 116617, Apr. 2021, doi: 10.1016/j.apenergy.2021.116617.
- [37] Y. Nishino, "Development of thermoelectric materials based on Fe₂ VAl Heusler compound for energy harvesting applications," *IOP Conf. Ser. Mater. Sci. Eng.*, vol. 18, no. 14, p. 142001, May 2011, doi: 10.1088/1757-899X/18/14/142001.

- [38] X. Chen, V. B. Naik, R. Mahendiran, and R. V. Ramanujan, "Optimization of Ni–Co–Mn–Sn Heusler alloy composition for near room temperature magnetic cooling," *J. Alloys Compd.*, vol. 618, pp. 187–191, Jan. 2015, doi: 10.1016/j.jallcom.2014.08.032.
- [39] J. P. Perdew, K. Burke, and M. Ernzerhof, "Generalized Gradient Approximation Made Simple," *Phys. Rev. Lett.*, vol. 77, no. 18, pp. 3865–3868, Oct. 1996, doi: 10.1103/PhysRevLett.77.3865.
- [40] P. Giannozzi *et al.*, "QUANTUM ESPRESSO: a modular and open-source software project for quantum simulations of materials," *J. Phys. Condens. Matter*, vol. 21, no. 39, p. 395502, Sep. 2009, doi: 10.1088/0953-8984/21/39/395502.
- [41] G. K. H. Madsen and D. J. Singh, "BoltzTraP. A code for calculating band-structure dependent quantities," *Comput. Phys. Commun.*, vol. 175, no. 1, pp. 67–71, Jul. 2006, doi: 10.1016/j.cpc.2006.03.007.
- [42] T. Jia, G. Chen, and Y. Zhang, "Lattice thermal conductivity evaluated using elastic properties," *Phys. Rev. B*, vol. 95, no. 15, p. 155206, Apr. 2017, doi: 10.1103/PhysRevB.95.155206.
- [43] M. K. Yadav and B. Sanyal, "First principles study of thermoelectric properties of Li-based half-Heusler alloys," *J. Alloys Compd.*, vol. 622, pp. 388–393, Feb. 2015, doi: 10.1016/j.jallcom.2014.10.025.
- [44] A. Togo, L. Chaput, and I. Tanaka, "Distributions of phonon lifetimes in Brillouin zones," *Phys. Rev. B*, vol. 91, no. 9, p. 094306, Mar. 2015, doi: 10.1103/PhysRevB.91.094306.
- [45] S. Matth, S. Pandey, and H. Pandey, "Ab-initio optimization of CoHfSi Half-Heusler alloy," *Mater. Today Proc.*, p. S2214785322075411, Dec. 2022, doi: 10.1016/j.matpr.2022.12.169.
- [46] S. Ahmad Khandy, K. Kaur, S. Dhiman, J. Singh, and V. Kumar, "Exploring thermoelectric properties and stability of half-Heusler PtXSn (X = Zr, Hf) semiconductors: A first principle investigation," *Comput. Mater. Sci.*, vol. 188, p. 110232, Feb. 2021, doi: 10.1016/j.commatsci.2020.110232.
- [47] S. A. Khandy *et al.*, "Strain dependent electronic structure, phonon and thermoelectric properties of CuLiX (X=S,Te) half Heusler compounds," *Phys. B Condens. Matter*, vol. 677, p. 415698, Mar. 2024, doi: 10.1016/j.physb.2024.415698.
- [48] Md. M. Islam and A. Zubair, "Ab initio study of uniaxial strain-induced thermoelectric property tuning of individual single-wall carbon nanotubes," *Mater. Adv.*, vol. 4, no. 24, pp. 6553–6567, 2023, doi: 10.1039/D3MA00713H.
- [49] R. S. Sunmonu, J. O. Akinlami, E. O. Dare, and G. A. Adebayo, "Effects of Y atom substitution on the structural, magnetic, electronic, elastic, mechanical, thermodynamic and thermoelectric properties of Co₂YAl (Y = Cr, Mn) Full Heusler alloys from first principles investigations," *Comput. Condens. Matter*, vol. 21, p. e00412, Dec. 2019, doi: 10.1016/j.cocom.2019.e00412.
- [50] B. Anissa, D. Radouan, B. Benaouda, and A. Omar, "First-principles study of structural, electronic, thermodynamic, and thermoelectric properties of a new ternary half-Heusler alloy PdZrGe," *Chin. J. Phys.*, vol. 56, no. 6, pp. 2926–2936, Dec. 2018, doi: 10.1016/j.cjph.2018.09.027.
- [51] S. A. Khandy and J.-D. Chai, "Strain engineering of electronic structure, phonon, and thermoelectric properties of p-type half-Heusler semiconductor," *J. Alloys Compd.*, vol. 850, p. 156615, Jan. 2021, doi: 10.1016/j.jallcom.2020.156615.
- [52] A. Saini, S. Nag, R. Singh, A. A. Alshaikhi, and R. Kumar, "Unraveling the effect of isotropic strain on the transport properties of half-Heusler alloy LiScGe," *J. Alloys Compd.*, vol. 859, p. 158232, Apr. 2021, doi: 10.1016/j.jallcom.2020.158232.
- [53] H. Alqurashi, R. Haleoot, and B. Hamad, "First-principles investigations of the electronic, magnetic and thermoelectric properties of VTiRhZ (Z= Al, Ga, In) Quaternary Heusler alloys," *Mater. Chem. Phys.*, vol. 278, p. 125685, Feb. 2022, doi: 10.1016/j.matchemphys.2021.125685.
- [54] K. Kaur and R. Kumar, "Giant thermoelectric performance of novel TaIrSn Half Heusler compound," *Phys. Lett. A*, vol. 381, no. 44, pp. 3760–3765, Nov. 2017, doi: 10.1016/j.physleta.2017.09.043.

- [55] S. Mahmoudi, M. M. Golzan, and E. Nemati-Kande, "Crystal structure, stability, and transport properties of Li₂BeAl and Li₂BeGa Heusler alloys: a DFT study," *Sci. Rep.*, vol. 14, no. 1, p. 12201, May 2024, doi: 10.1038/s41598-024-63092-x.
- [56] B. Anissa, D. Radouan, B. Benaouda, and A. Omar, "First-principles study of structural, electronic, thermodynamic, and thermoelectric properties of a new ternary half-Heusler alloy PdZrGe," *Chin. J. Phys.*, vol. 56, no. 6, pp. 2926–2936, Dec. 2018, doi: 10.1016/j.cjph.2018.09.027.
- [57] O. M. Abid *et al.*, "Structural, electronic, elastic, thermoelectric and thermodynamic properties of the NbMSb half heusler (M=Fe, Ru, Os) compounds with first principle calculations," *Superlattices Microstruct.*, vol. 93, pp. 171–185, May 2016, doi: 10.1016/j.spmi.2016.01.001.
- [58] Berzelius LJ, Arago F, Einstein A, "THE DULONG-PETIT LAW OF SPECIFIC HEATS".
- [59] A. A. Musari, "Electronic, mechanical, vibrational and thermodynamic properties of FeXSb (X = Hf and Nb) Half-Heusler alloys from first-principles approach," *Solid State Sci.*, vol. 122, p. 106755, Dec. 2021, doi: 10.1016/j.solidstatesciences.2021.106755.
- [60] G. Xing, J. Sun, Y. Li, X. Fan, W. Zheng, and D. J. Singh, "Electronic fitness function for screening semiconductors as thermoelectric materials," *Phys. Rev. Mater.*, vol. 1, no. 6, p. 065405, Nov. 2017, doi: 10.1103/PhysRevMaterials.1.065405.
- [61] Z. Feng, Y. Fu, A. Putatunda, Y. Zhang, and D. J. Singh, "Electronic structure as a guide in screening for potential thermoelectrics: Demonstration for half-Heusler compounds," *Phys. Rev. B*, vol. 100, no. 8, p. 085202, Aug. 2019, doi: 10.1103/PhysRevB.100.085202.
- [62] T. M. Ashani, P. O. Adebambo, F. Ayedun, I. O. Osinuga, M. A. Idowu, and G. A. Adebayo, "The effective mass, fitness function and enhanced thermoelectric properties in CuSbS₂ for p-type thermoelectric material applications: Density functional theory approach," *Mater. Sci. Eng. B*, vol. 273, p. 115404, Nov. 2021, doi: 10.1016/j.mseb.2021.115404.